# Generation of non-adiabatic flamelet manifolds: comparison of two approaches applied on a single-element $GCH_4/GO_2$ combustion chamber

*Paola Breda*[⋆†] *and Michael Pfitzner*[⋆]
*Nikolaos Perakis*[⋆⋆] *and Oskar Haidn*[⋆⋆]
[⋆] *Chair of Thermodynamics, Bundeswehr University of Munich,*
*Werner-Heisenberg-Weg 39, 85579 Neubiberg, Germany*
[⋆⋆] *Chair of Turbomachinery and Flight Propulsion, Technical University of Munich*
*Boltzmannstrasse 15, 85748 Garching, Germany*
paola.breda@unibw.de · michael.pfitzner@unibw.de · nikolaos.perakis@ltf.mw.tum.de · oskar.haidn@ltf.mw.tum.de
[†]Corresponding author

## Abstract

This work aims to compare two non-adiabatic flamelet combustion models for the simulation of a subscale single-injector $GCH_4/GO_2$ combustion chamber in rocket-like operative conditions. The role of chemistry in terms of recombination reactions at the chamber wall is influenced by the choice of the enthalpy space and the scalar dissipation rate model across the flamelets, with a strong dependence observed for the first item. One non-adiabatic flamelet model was able to correctly predict the heat transfer at wall. The second model however foresaw higher recombination effects in the low-enthalpy regions, resulting in a higher wall heat flux exceeding the experimental data. Remapping the second enthalpy space onto the first one helped to recover the discrepancy.

## Introduction

The space industry and the research community recently focused on methane as suitable candidate to substitute hydrogen in liquid rocket engine (LRE) propulsion systems, since it offers several benefits. It is easier and safer to store, contributing to reduce the operative costs and increasing the ecological impact. Its higher density allows to further contain the tank volume in favor of a more compact stage. Moreover, methane presents better cooling properties for rocket engines since its molar heat capacity is higher than hydrogen[1] .
Combustion of $CH_4/O_2$ at high pressure is however still an open field of research. Higher chamber pressure leads to improved vehicle performance, which also turns into an increase of heat transfer at wall. A critical requirement during the design phase of a LRE is the accurate prediction of the thermal loads at the chamber wall. Using hydrocarbon fuels instead of hydrogen directly impacts the computational cost required by CFD simulations of turbulent reactive flows in this phase. A typical detailed mechanism for methane/air combustion involves 200 species and 1000 reactions, covering a wide spectrum of chemistry modes[2] . This results in a stiff chemical system to be solved at run-time, which is unaffordable for practical use in the industry where a trade-off between simulation accuracy and computational time is an asset.
Chemistry tabulation methods allow to remove the chemistry integration step at run-time by tabulating the thermochemical properties of the reactive flow in advance. The tabulations presented in this work rely on the fast-chemistry assumption, where the chemistry is assumed to almost instantaneously adapt to any flow perturbation and is therefore decoupled from the physical scales. The turbulent flame can be seen as a collection of laminar flames, named flamelets, described by a mixing parameter[3] , eventually extended to include a reactive progress variable[4 5] .
The strong temperature gradients between the hot gases and the coolant at the walls of a LRE combustion chamber cause enthalpy losses which must be accounted for in the flamelet model. It is common practice to assume the chemistry frozen at walls, where only the temperature is reduced by the flame/wall interaction. In such models the recombination processes are not contemplated. In order to capture the effect of heat losses on the hot mixture several implementations were suggested by the research community in the past years, among which the use of head-on[6] and side-wall[7] quenching. The latter was successfully tested for $H_2/O_2$ high pressure combustion[8 9] and recently adopted

for $CH_4/O_2$ flames[10 11] . This model will be used in this work as first tabulation method for comparison.
Alternatively, an empirical enthalpy profile characterizing the heat losses can be assigned a priori[12] . The flame structure is constrained to the assigned enthalpy level by means of an extra heat loss sink term in the flame energy equation[13] , or by means of an operation splitting technique between the chemistry and the diffusion terms[14] . The latter approach is used in this work as second tabulation method.
The two non-adiabatic flamelet implementations, integrated respectively in OpenFOAM[15] and Cantera[16] , are tested on a subscale $GCH_4/GO_2$ single-injector combustion chamber operating under LRE-like conditions[17] . A fully resolved hybrid LES/RANS turbulent model is chosen for the OpenFOAM simulations. The paper is organized as follows. The governing equations for the turbulence modeling are reported in Section I. An introduction to the flamelet combustion model and its non-adiabatic extension is given in Section II, followed by a detailed comparison of the two models object of this work. The test case and numerical set up are described in Section III. Finally the results of the CFD simulations are reported and commented in Section IV.

## I. Turbulence Model

An Improved Delayed Detached Eddy Simulation (IDDES) hybrid model[18] was selected for the 3D simulations, where a blending function determines the switch between the LES solver, mainly active in the core flow, and the RANS solver active in wall proximity. The Favre-filtered governing equations for mass and momentum read

$$\frac{\partial \bar{\rho}}{\partial t} + \frac{\partial \bar{\rho}\tilde{u}_i}{\partial x_i} = 0 \tag{1}$$

$$\frac{\partial \bar{\rho}\tilde{u}_i}{\partial t} + \frac{\partial \bar{\rho}\tilde{u}_i\tilde{u}_j}{\partial x_j} = -\frac{\partial \bar{p}}{\partial x_i} + \frac{\partial}{\partial x_i}(\bar{\tau}_{ij} - \bar{\rho}(\widetilde{u_i u_j} - \widetilde{u}_i\widetilde{u}_j)) \tag{2}$$

with the symbols $\tilde{\star}$ and $\bar{\star}$ denoting respectively the density-weighted and the unweighted filtered quantities. $\widetilde{u}_i$ is the $i$-th component of the filtered velocity, $\bar{\rho}$ and $\bar{p}$ the averaged fluid density and pressure. The strain rate tensor $\bar{\tau}_{ij}$ is simplified by the gradient diffusion hypothesis, while the unresolved Reynolds stresses $\widetilde{u_i u_j} - \widetilde{u}_i\widetilde{u}_j$ are closed by the Smagorinsky sub-grid scale (SGS) model.
The energy equation in terms of absolute enthalpy $\widetilde{h}$ is transported as

$$\frac{\partial \bar{\rho}\tilde{h}}{\partial t} + \frac{\partial \bar{\rho}\tilde{u}_i\tilde{h}}{\partial x_i} = -\lambda\,\frac{\partial T}{\partial x} - \frac{\partial}{\partial x_i}\left(\left(\frac{\bar{\mu}}{Pr} + \frac{\mu^{sgs}}{Pr_t}\right)\frac{\partial \tilde{h}}{\partial x_i}\right) \tag{3}$$

with $\lambda$ the thermal conductivity, $\bar{\mu}$ the molecular and $\mu^{SGS}$ the subgrid dynamic viscosities. The diffusion coefficients were derived from the Fick's law assuming unity Lewis numbers. Thermal diffusion and radiation are neglected. The dimensionless Schmidt (Sc) and Prandtl (Pr) numbers are set to $Sc_t$ = Sc = $Pr_t$ = Pr=1. The mixture viscosity and thermal diffusion are evaluated from the Sutherland transport model and the $c_p$ from the Janaf NASA polynomials. The ideal gas equation of state is used to retrieve the density.
The Spalart-Allmaras (SA) equation was chosen to transport the artificial kinematic viscosity $\tilde{\nu}$ in the RANS active region, from which the eddy viscosity is computed as $\nu_T = \tilde{\nu}\, f_{v1}$. The equation reads

$$\frac{\partial \tilde{\nu}}{\partial t} = C_{b1}(1 - f_{t2})\tilde{S}\,\tilde{\nu} + \frac{1}{\sigma}\left(\frac{\partial}{\partial x_i}\left((\nu + \tilde{\nu})\,\frac{\partial \tilde{\nu}}{\partial x_i}\right) + C_{b2}\frac{\partial^2 \tilde{\nu}}{\partial x_i^2}\right) - \left(C_{w1}\, f_w - \frac{C_{b1}}{k^2} f_{t2}\right)\left(\frac{\tilde{\nu}}{d}\right)^2 + f_{t1}\Delta U^2 \tag{4}$$

where the $C_i$ coefficients and empirical functions $f_j$ are assigned from the original formulation[19] .
In order to avoid a premature switching in the boundary layer region and to overcome a possible mismatch of the boundary layers at the interface, the turbulence length scale for transition is defined as

$$l = \tilde{f_d}(1 + f_e)\, l_{RANS} + (1 - \tilde{f_d}) l_{LES} \tag{5}$$

with $\tilde{f_d}$, $f_e$ being the blending functions which ensure a smooth transition between LES and RANS. The reader is pointed to the original formulation for further details[18] .

## II. Combustion Model

### Adiabatic Flamelets

In LRE the fuel and oxidizer are injected separately and are simultaneously subjected to mixing and burning. The non-premixed combustion is strongly dependent on diffusion processes, as molecular diffusion of the reactants towards the stoichiometric zone is slower than most chemical reactions. In the flamelet model the turbulent flame can be seen as an ensemble of laminar diffusion flames, as depicted on the left side of Fig. 1.
The flame structure in terms of species mass fractions $Y_k$ and temperature $T$ is a function of the mixture fraction $f$, a passive scalar representative of the mixing between fuel and oxidizer. Its value is usually set to 1 at the fuel inlet and to 0 at the oxidizer inlet. The transport equation for species and enthalpy in physical space is subjected to the transformation $\partial Y_k/\partial x_i = \partial Y_k/\partial f \cdot \partial f/\partial x_i$, with the assumption that the flame structure is normal to the flame front. The flamelet equations in mixture fraction space therefore read

$$\rho\frac{\partial Y_k}{\partial t} - \frac{\chi\rho}{2}\frac{\partial^2 Y_k}{\partial f^2} = \dot{\omega}_k \tag{6}$$

$$\rho\frac{\partial h_s}{\partial t} - \frac{\chi\rho}{2}\frac{\partial^2 h_s}{\partial f^2} = -\sum_{n=1}^{k} h_k\,\dot{\omega}_k \tag{7}$$

with $\dot{\omega}_k$ the production rate and $h_k$ the standard enthalpy of formation of species $k$, $h_s$ the mixture sensible enthalpy. The scalar dissipation rate $\chi$ is the inverse of a diffusion time scale and delimits the stable combustion regime. Its instantaneous value depends on the thermal diffusivity $D$ and the mixture fraction gradient:

$$\chi = 2D\,|\nabla f|^2 \tag{8}$$

The above equations could be derived in absence of differential diffusion and Lewis numbers $\mathrm{Le}_k$=1. In this work, the analytical profile for $\chi$ is taken from the original formulation[3] as

$$\chi = \chi_{st}\exp[2(\mathrm{erfc}^{-1}(2\,f_{st})^2) - 2(\mathrm{erfc}^{-1}(2\,f)^2] \tag{9}$$

unless otherwise specified. The instantaneous $\chi_{st}$ is evaluated at the stoichiometric $f_{st} = 0.2$ (for $CH_4/O_2$ combustion), while $\mathrm{erfc}^{-1}$ is the inverse error function.

### Non-adiabatic Flamelets

Enthalpy losses can be integrated in the database by inducing fuel-side quenching on the flamelets as shown on the right side of Fig. 1. A permeable, isothermal and chemically inert wall is placed on the fuel-rich side starting at location $f_{wall}$ and shifted from the fuel inlet $f = 1$ to the flame front $f_{st}$ for each new flamelet generation. The wall temperature $T_{wall} < T_{fuel}$ can be also reduced at each step, to extend the manifold towards the low-enthalpy region.
The first table used for comparison was generated based on this model and it labeled hereafter as B. Eq. 7-6 are solved in OpenFOAM for the complete domain $0 < f < 1$. The temperature behavior for the cells in $f_{wall} < f < 1$ is recovered by linearly interpolating towards the fuel temperature. The analytical profile for $\chi$ is scaled to include the wall presence[8]

$$\chi = \chi_{st}\exp[2(\mathrm{erfc}^{-1}(2\,f_{st}/f_{wall})^2) - 2(\mathrm{erfc}^{-1}(2\,f/f_{wall})^2] \tag{10}$$

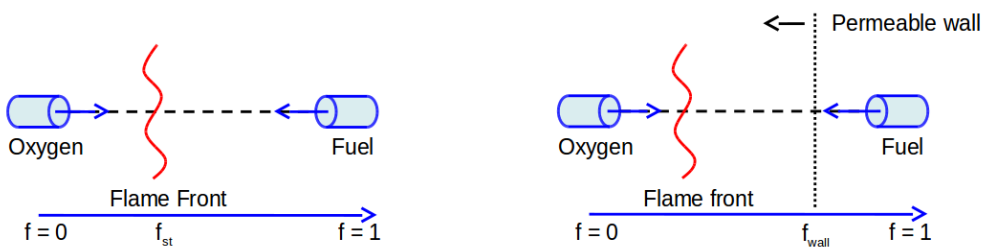


Figure 1: Adiabatic counterflow diffusion flame (left) and introduction of side-wall quenching (right)

with $\chi_{st} = 1\text{s}^{-1}$ fixed for all calculations. The database is constructed on $CH_4/O_2$ flamelets at 20 bar and inlet temperature of respectively 269 K and 278 K, according to the operative conditions of the test case. A 17 species mechanism[20], derived from GRI-1.2[21] via the direct relation graph theory, sensitivity analysis and computational single perturbation, was used for both manifolds and the IDDES simuations. The influence of the wall on the flame structure for case B is shown on the left column of Fig. 2. The adiabatic temperature profile (in red) shifts towards quenching (in blue) as enthalpy losses increase due to the wall presence. This process favors the recombination of CO towards $CO_2$, as can be seen in the fuel-rich mixture. The lowest admissible temperature in the table is capped to 200 K to ensure the look-up of physical admissible thermo-chemical properties. The upper and lower enthalpy boundaries $h_{max}$ and $h_{min}$ are further extended to frozen states[11] to provide a sufficient margin to the table boundaries during the CFD simulation. The normalized absolute enthalpy is defined as

$$h_{norm} = \frac{h - h_{min}}{h_{max} - h_{min}} \tag{11}$$

and used as look-up parameter. It is worth to notice that quenching phenomena due to flame strain are not included in this work. Maximum values of $\chi \approx 10\,000\,\text{s}^{-1}$ still far from the extinction were observed in previous simulations at the shear-layer close to the injector plate[22], whereas $\chi < 1\text{s}^{-1}$ was detected elsewhere. Since the focus of the simulation is targeted to the wall-heat flux prediction thus far from the injector, the single $\chi$ assumption is justified.

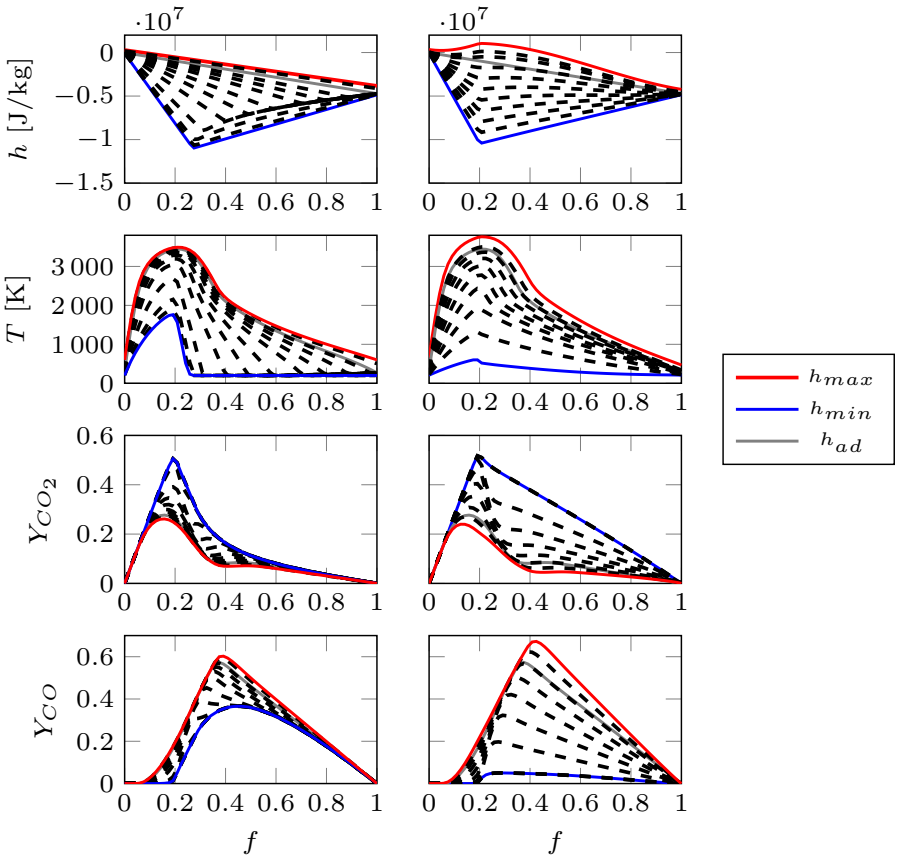


Figure 2: Effects of enthalpy losses on $T$, $CO_2$, $CO$ towards quenching for $\chi_{st} = 1\text{s}^{-1}$. Comparison between method-B (left) and method-PO (right). Profiles corresponding to maximal enthalpy in red, minimum in blue

The second flamelet model is referred as PO in the following sections. Eq. 7 is replaced by imposing enthalpy profiles as an equality constraint for $f$. Such profiles are assigned a priori, based on an empirical distribution as function of $f$. The boundary value problem for the diffusion and kinetic terms of Eq. 6 is solved via an operation splitting technique. The algorithm was implemented in Matlab using Cantera libraries for the chemistry. The reader is referred to the original paper[14] for further details. The $\chi$ distribution from Eq. 9 is imposed in this case. Enthalpy profiles and flame

structure can be seen on the right column of Fig. 2. For completeness, the adiabatic flamelet (solid line) is shown as reference, although the state is not directly included in this table. The enthalpy space extends to higher values of absolute enthalpy, and the minimum of the loss profiles is shifted towards the stoichiometric $f_{st} = 0.2$ compared to model B. The temperature covers a wider region through the cold mixture within $0 < f < 0.2$. CO recombination towards $CO_2$ is significantly stronger and affects the fuel-rich mixture for $f > 0.7$. Such effects are not seen with model B.
Table 1 summarizes the major differences between the two models. A third case, named PM, consists of flamelets generated with the PO method by imposing the $h$ profiles of B (top-left of Fig. 2). The table also reports the amount of flamelets produced by both models within 24 hours and parallelized on $n$ cores. The optimized libraries included in the Cantera package allow a massive speed-up of model PO compared to the OpenFOAM solver of B.

Table 1: Summary of the non-adiabatic flamelet table features

| | **Enthalpy loss** | $\chi$ **model** | $f \times h_{norm}$ **grid** | **#flamelets**[a] |
|---|---|---|---|---|
| B | permeable wall[7] | Eq. 10 | $202 \times 50$ | $n$ |
| PO | target enthalpy profile[12] | Eq. 9 | $150 \times 50$ | $8.3 \times n$ |
| PM | target enthalpy profile from B | Eq. 10 | $150 \times 50$ | $8.3 \times n$ |

[a]produced in 24h on $n$ cores

**Turbulence-Chemistry Interaction**

In the IDDES turbulence model the Favre-filtered quantities are subjected to a low-pass filter. The flame structure in terms of $Y_k$ and $T$ can be generalized by the quantity $\Phi$, so that it can be parametrized on the manifold as $\Phi(f, h_{horm})$. Its value is therefore integrated over a presumed probability density function (PDF) $\tilde{P}(f, h_{norm})$ as

$$\widetilde{\Phi} = \int\int \Phi(f, h_{norm})\, \widetilde{P}(f, h_{norm})\, df\, dh_{norm} = \widetilde{\Phi}(f, \widetilde{f''^2}, h_{norm}) \tag{12}$$

In the PDF the variables are assumed statistically independent and described as

$$\widetilde{P}(f, h_{norm}) = \beta(f; \tilde{f}, \widetilde{f''^2}) \cdot \delta(\widetilde{h}_{norm} - h_{norm}|f) \tag{13}$$

A presumed $\beta-$PDF is used to model the mixture fraction distribution while a $\delta$-function is used for enthalpy. In addition to Eq. 1-4, the filtered mixture fraction $\tilde{f}$ is transported in OpenFOAM as key parameter for the flamelet tabulation, together with its variance $\widetilde{f''^2}$ describing the unresolved fluctuations

$$\frac{\partial \bar{\rho}\tilde{f}}{\partial t} + \frac{\partial \bar{\rho}\tilde{u}_i\tilde{f}}{\partial x_i} = \frac{\partial}{\partial x_i}\left(\left(\frac{\bar{\mu}}{Sc} + \frac{\mu^{sgs}}{Sc_t}\right)\frac{\partial \tilde{f}}{\partial x_i}\right) \tag{14}$$

$$\frac{\partial \bar{\rho}\widetilde{f''^2}}{\partial t} + \frac{\partial \bar{\rho}\tilde{u}_i\widetilde{f''^2}}{\partial x_i} = \frac{\partial}{\partial x_i}\left(\left(\frac{\bar{\mu}}{Sc} + \frac{\mu^{sgs}}{Sc_t}\right)\frac{\partial \widetilde{f''^2}}{\partial x_i}\right) - 2\,\bar{\rho}\tilde{\chi} + 2\left(\frac{\tilde{\mu}}{Sc} + \frac{\mu^{sgs}}{Sc_t}\right)\left(\frac{\partial \tilde{f}}{\partial x_i}\right)^2 \tag{15}$$

The last equation is taken from Kemenov et al.[23] , whereas the scalar dissipation rate $\chi$ is solved analytically according to Domingo et al.[24]

$$\tilde{\chi} = \frac{\tilde{\mu}}{\bar{\rho}\,Sc}\left(\frac{\partial \tilde{f}}{\partial x_i}\right)^2 + \frac{C_\chi\,\mu^{sgs}}{2\,\bar{\rho}\,Sc_t}\frac{\widetilde{f''^2}}{\Delta^2} \tag{16}$$

## III. Test Case and Numerical Setup

The subscale single-element combustion chamber for gaseous $CH_4/O_2$ operated at the Technical University of Munich was designed in the context of the research program SFB/TR-40 with the aim of providing experimental data for the wall heat flux in order to validate CFD tools[17 25] . The test campaign at 20 bar nominal pressure and mixture ratio ROF = 2.6 was selected for this work, as already object of numerous studies[22 26 27 28 29 30] . The schematic view in Fig. 3 shows the single co-axial injector centered at the faceplate and the characteristic squared cross-section of this chamber, with dimensions $12{\times}12\,mm^2$. The chamber length from faceplate to nozzle throat is 303 mm. The hot gas expands through a nozzle having contraction ratio 2.5. Since the combustion chamber is capacitively cooled, it can be operated

for a short time (typically 3 s). Equally spaced pressure transducers provide measurements for the pressure profile along the chamber axis, whereas thermocouple readings allow to reconstruct the wall heat flux. Optical diagnostics of OH* close to the injector plate were recently published for this chamber[31] . The inflow boundary conditions are reported in details in Table 2.

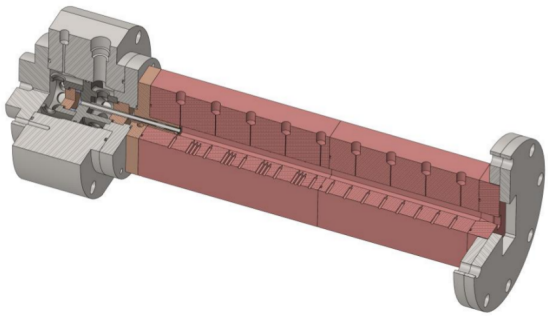

Figure 3: Experimental setup: single-injector combustion chamber

The computational domain for the CFD simulations is cut at the axial position x = 272.5 mm, since no experimental data are available for the nozzle segment. The injector is not included in the domain and the inlets are patched at the faceplate. A prescribed temperature profile from the experiment acts as boundary condition at walls, except from the faceplate and the post-tip which are treated adiabatically. A fixed pressure value is assigned at outlet, corresponding to the reading of the last pressure transducer (18.216 bar). Inflow turbulence is applied in form of digital filters[32] with an isotropic turbulence value assigned to 3%. The filtered fields are averaged over 10 ms, which corresponds to a 5 times flow-through. The pressure-velocity coupling is treated by a PISO solver, modified for table interpolation. The time step is adjusted to a maximum Courant-Friedrichs-Lewy (CFL) number of 0.4. Second order schemes were chosen for the divergence terms: the Total Variation Diminishing (TVD) Van-Leer for the scalar fields, the OpenFOAM unbouded Gauss linear for the velocity field. The time discretization is done via a first order Implicit Euler scheme.

Table 2: Injector geometry and inflow properties

| | **Fuel Stream** | **Oxidizer Stream** |
|---|---|---|
| Geometry [mm] | $D_{inner} = 5$ | $D = 4$ |
| | $D_{outer} = 6$ | |
| Mass flow rate [kg/s] | 0.017 | 0.045 |
| Velocity [m/s] | 130 | 127 |
| Temperature [K] | 269 | 278 |
| Pressure [bar] | 20 | 20 |
| Reynolds (Re) | 186321 | 722775 |

**Mesh Study**

In order to select the suitable mesh for the final simulations, the accuracy of two sub-domains were investigated separately, i.e. the core flow and the boundary layer. The SA Eq. 4 for the IDDES requires $y^+ \leqslant 1$. In a first attempt, a coarse mesh of about $6{\times}10^6$ (6M) cells and $y^+ > 1$ at walls was used to initialize the simulation with the flamelet set from B. In a second step the mesh was refined in each direction with an increase in cells of factor $2^3$, guaranteeing $y^+ < 1$ at wall and a posttip resolution of 10 cells. This resulted in a finer mesh of about 53M cells. A qualitative comparison of the core and wall fields in axial direction is shown for model B in Fig. 4. The mean temperature and its fluctuation along the chamber axis characterize the core flow. The profile of the refined mesh is shifted downwards, indicating a weaker mixing process in the core. However the pressure and wall heat flux distribution at wall are more suitable to indicate the quality of the mesh, because they are directly comparable with the experimental data. It is straightforward to conclude that the refined mesh is able to capture the pressure and the wall heat flux very well and is therefore selected for the following simulations. An intermediate mesh of 30M is object of current investigation, in the effort to reduce the computational cost required by the 53M mesh.

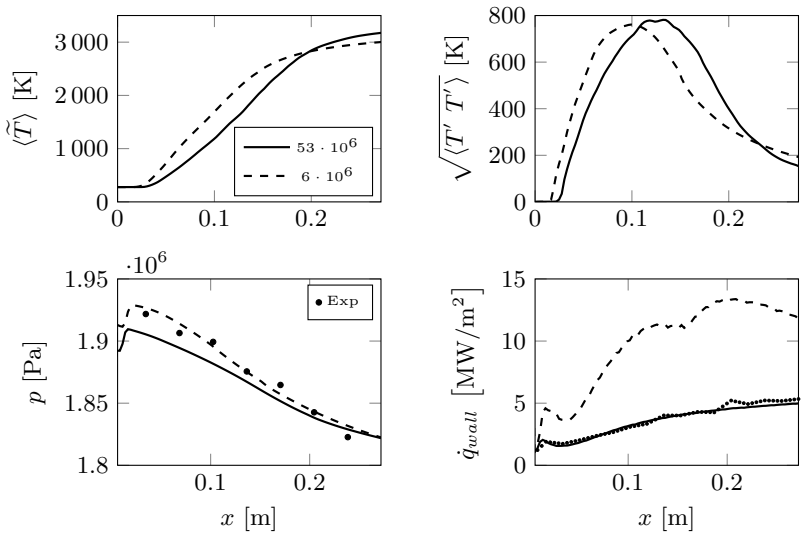


Figure 4: Coarse and refined mesh comparison. On the top: averaged filtered $\tilde{T}$ and its fluctuations sampled along the center line. On the bottom: axial $p$ and $\dot{q}_{wall}$ profiles compared to the experiment

## IV. Results

Here the results obtained for models B and PO are discussed. An additional simulation (PM) was ran to demonstrate that the model PO can reproduce exaclty the results of B, if the same enthalpy space is used.

**Flame Structure**

The averaged mixture fraction, temperature and $O_2$ fields in axial direction are shown in Fig. 5 (B on the top, PO on the bottom of each figure). The mean $\tilde{f}$ field (top) reveals the presence of a thin layer of colder fuel at walls characterized by $f = 0.3$. Within the first 10 mm, the fuel jet of simulation B almost extends to the wall, while in PO it mixes with the hot gases before reaching it. The impact of the hot gas at wall generates a recirculation zone close to the faceplate corners. A visual analysis of the mean fields along the combustion chamber axis can also reveal the degree of mixing generated by the turbulence model, in this case a LES in the core flow. The mixing process can play a relevant role for the wall heat flux prediction, as already observed in previous LES studies[27 29]. The length of the $O_2$ core is a good indicator for mixing: the longer the core, the weaker the mixing process, resulting in a less efficient combustion process and a lower heat transfer at wall. On the bottom of Fig. 5 the length of the oxidizer core for both simulations is estimated to be 150 mm, slightly shorter for model PO. This is reflected in a similar way by the mean temperature fields (middle). Both models predict a maximum temperature close to 3200 K and in both cases unburned oxygen exists the domain with a concentration of $Y_{O2} = 0.1$, denoting incomplete combustion. It should be kept in mind however that the computational domain was cut prior the nozzle segment. Whether the turbulence model has a larger effect on the heat transfer at wall than the tabulated flamelet models will be discussed in the subsequent section. Overall it can be concluded that the flame structure properties in the core flow do no vary significantly between the two models.
The development of the thermal boundary layer can be followed through the cross-sections as given in Fig. 6. Opposite to a circular cross-section, the thermal layer is strongly affected by the squared shape. The averaged $\widetilde{T}$ is shown on the bottom row while the instantaneous $\widetilde{T}$ on the top, with the left side corresponding to model B and the right side to model PO. Axial positions at x=10, 100, 200 mm were selected for comparison. At location x=10 mm, close to the faceplate, the injector geometry is visible, with a thin reaction zone concentrated at the shear layer. A thicker flame can be detected in the snapshot and in the mean fields of PO. Moving to x = 100 mm, it is evident how turbulent mixing preveals and the hot gases starts penetrating the oxygen core. The hot gases expands radially but are constricted by the squared cross-section, as reflected by their shape. It is also worth to notice the agglomeration of unburned gas at wall, expecially at the chamber corners. Further downstream at x = 200 mm the combustion gases have fully adapted to the square geometry, however methane is still present in the corners. The thermal boundary layer is perceptibly thinner for model PO, which might signal higher chemical activity in the wall proximity.

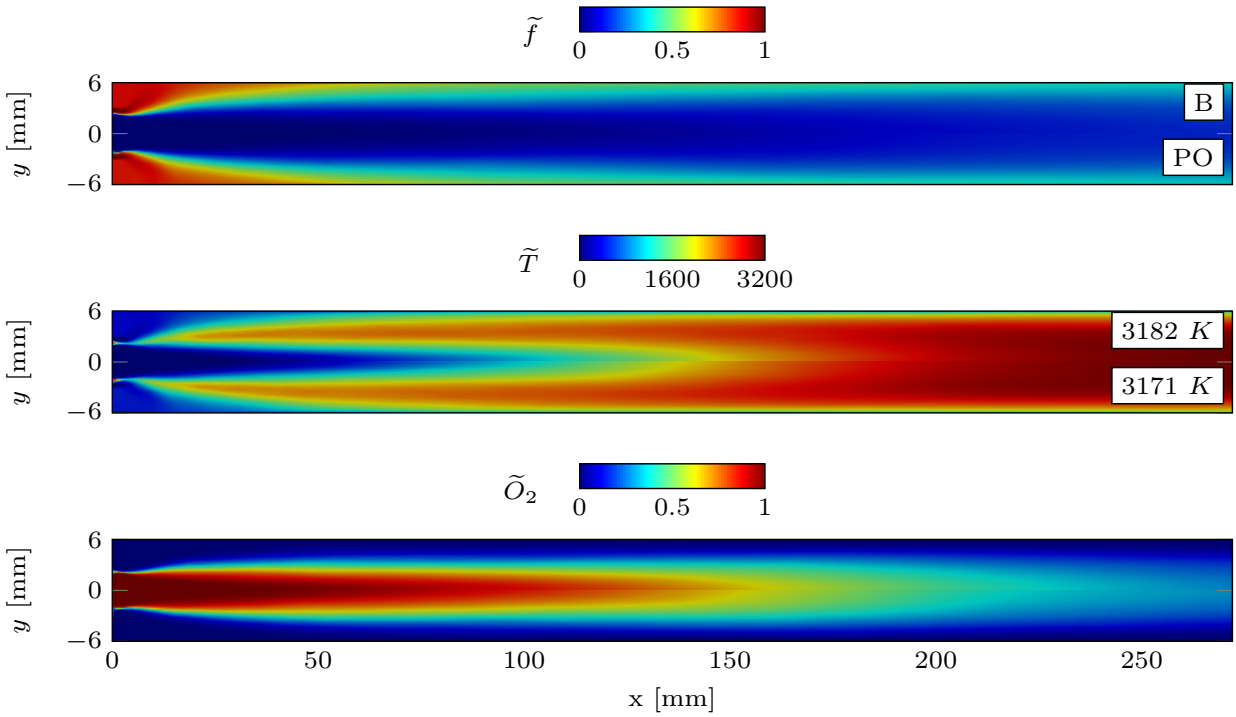


Figure 5: From the top: averaged $\widetilde{f}$, $\widetilde{T}$ and $\widetilde{O}_2$. Top half of each figure: method B. Bottom half: method PO

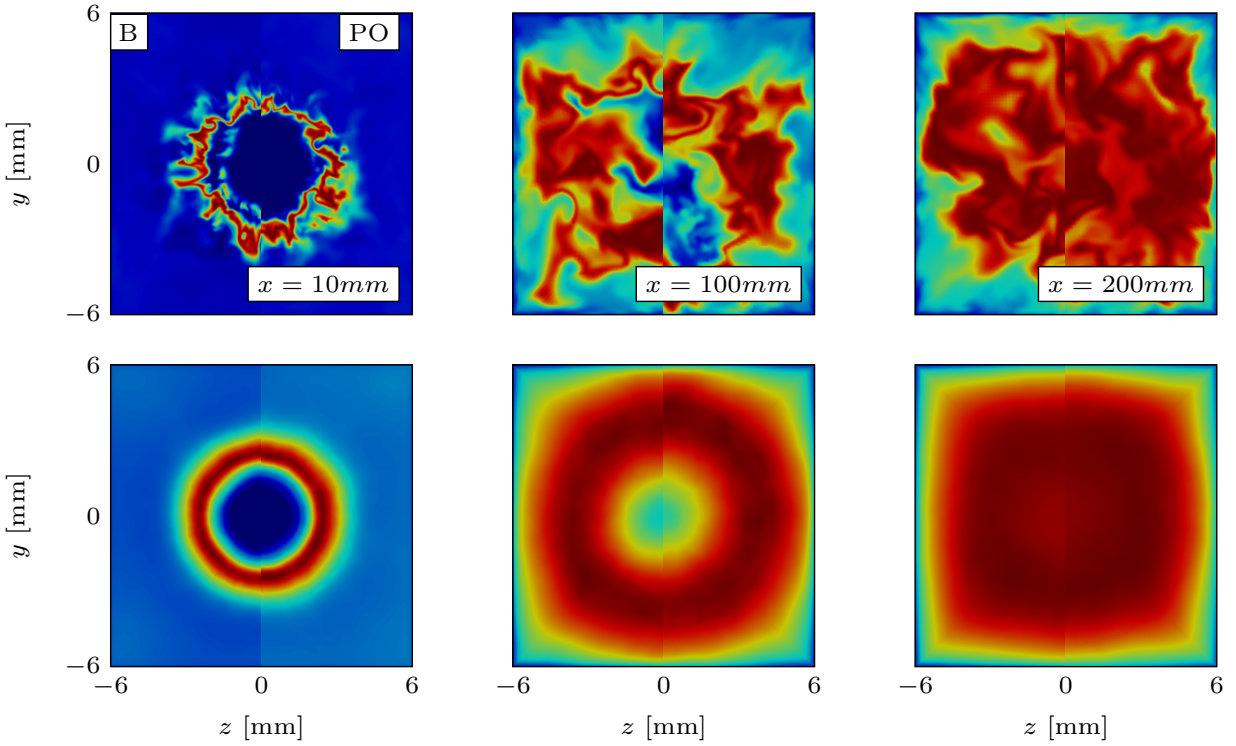


Figure 6: Snapshot on top and averaged $\widetilde{T}$ field on the bottom. Left side: method B. Right side: method PO

So far no major differences were detected between the two models. Investigating the instantaneous fields of normalized enthalpy and two major species (Fig. 7) however reveals interesting information about the composition space accessed by both tables. The top figure shows the transported values for the second table parameter, the normalized enthalpy. The $\widetilde{h}_{norm}$ space accessed in the core flow from model B is close to the upper boundary ($h_{norm} = 1$) almost everywhere

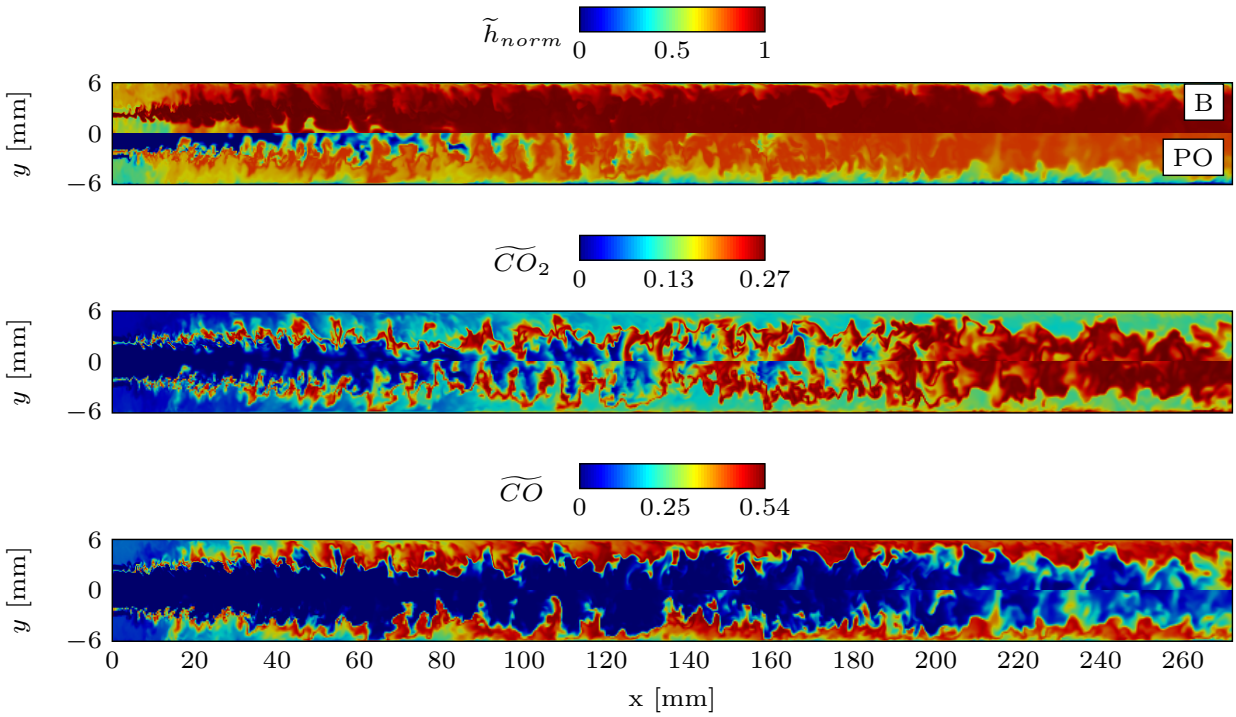


Figure 7: From the top: snapshot of fields $\widetilde{h}_{norm}$, $\widetilde{CO}_2$, $\widetilde{CO}$. Top half of each figure: method B. Bottom half: method PO

in the domain, while only at wall it drops to lower values due to the heat loss effects. This is because $h_{max}$ was chosen close to the adiabatic flamelet profile $h_{ad}$, as seen in Fig. 2. In model PO, $h_{max}$ was assigned far from the adiabatic flamelet profile, resulting in $h_{norm}$ clustered around 0.8 in the core flow, where the local adiabatic flame state should be found. Major losses are forseen close to the walls, as expected. Significantly different is the recombination process for model PO. In the second half of the domain, a higher concentration of $CO_2$ at walls can be seen in the middle figure for PO, leading to the conclusion that recombination reactions are dominant at wall. This effect was already detected in a 2D-RANS simulation of the same test case[28] , leading to results close to the chemical equilibrium (full recombination). The bottom figure confirms the decrease in CO while recombinating towards $CO_2$ at wall. At this point it appears justified to claim that the turbulent mixing derived by the IDDES model plays a smaller role in the wall heat flux prediction than the choice of the non-adiabatic flamelet manifold, at least in this work.
Recalling Fig. 2, both manifolds include recombination processes. The selection of the $\chi$ distribution for the generation of the flamelet database seems to play a role for this study but also the selection of the specific enthalpy profiles has an influence on the degree of recombination, since the normalized enthalpy will be determined by the maximum and minimum profiles imposed. In a parallel study subject to future publication, the same test case was simulated with model B and Eq. 9. It was found that the wall heat flux profile is weakly dependent on the $\chi$ model adopted for the generation of the flamelet manifold. Although the major products recombine stronger when using Eq. 9 instead of 10, the chemical states are still far away from the chemical equilibrium. This leads to the conclusion that the current results must have a stronger correlation to the selection of the enthalpy space enclosing the admissible thermo-chemical states. To prove the validity of this assumption, the third simulation (PM) was run. The target enthalpy profiles for the manifold generation were taken from B and the same $\chi$ model was applied. The results were found coincident with case B as it will be seen in the comparison with the experimental data.

**Scatter Plots**

It was shown from a detailed LES simulation[22] that the combustion regime close to the injector is dominated by diffusion processes, with $\chi$ values still far from the extinction condition. This is confirmed from Fig. 8, where scatter plots for temperature, main species and the enthalpy levels are shown for cross section x=10 mm (left hand side columns). The color scale represents the local $h_{norm}$ relative to each simulation. The left column shows the results for B, the right column for PO. An adiabatic flamelet for $\chi = 10\ 000\ s^{-1}$ is superimposed.
A deviation of the scatter plots from the fuel-rich flamelet solution in $0.4 < f < 0.8$ is expected, since the manifolds

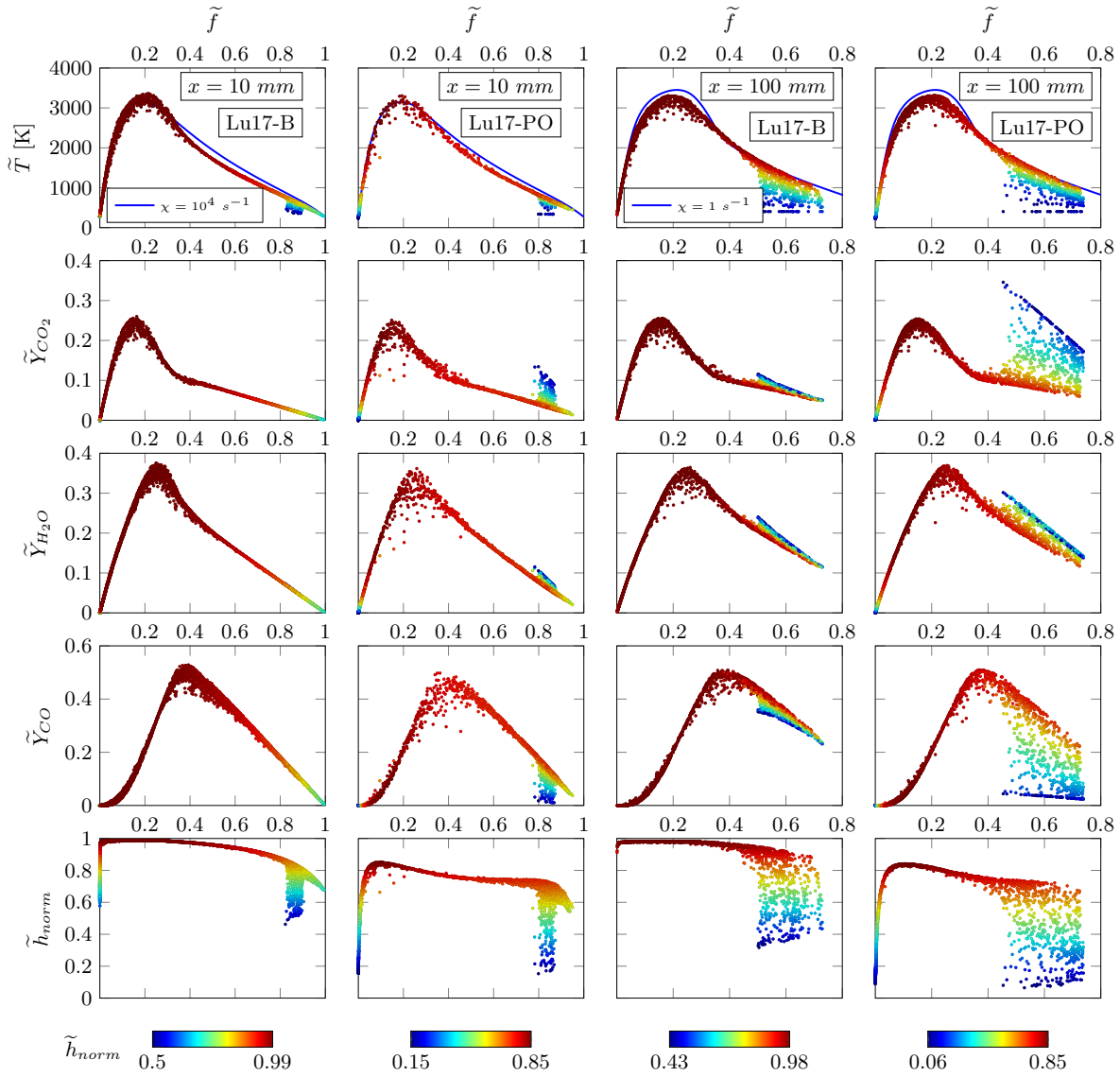


Figure 8: Scatter plots for temperature, major species and enthalpy at cross sections x=10,100 mm. Colormap is $\widetilde{h}_{norm}$

were constructed for a single value of $\chi = 1\,\mathrm{s}^{-1}$. Again, the limitation is accepted for this case, since the main focus is at wall where the $\chi$ drops to values below unity. The clustered points at lower temperature around $f = 0.8$ are located in proximity of the chamber walls where flow recirculation occurs, with $CO_2$ already abundant in PO and the hydrogen chemistry slighlty unbalanced towards $H_2O$ recombination. On the other side the heat losses are not affecting the chemical state of simulation B, and less scattering is present around stoichiometry.
The right hand side columns of Fig. 8 report the scatter plots for x=100 mm. Another adiabatic flamelet for $\chi = 1\,\mathrm{s}^{-1}$ is superimposed, revealing that lower temperatures are predicted by the simulations in the flame proximity. This could be a symptom of stronger dissipation originated by the IDDES model and is subject of future study. The gap between the flamelet and the scatter data for $0.4 < f < 0.8$ is absent, recovering the validity of the manifolds for a single strain rate. Recombination effects are here visible for both models, but stronger in PO. Within the range $0.5 < f < 0.7$ almost all CO recombines towards $CO_2$, but it is not fully consumed, indicating that the chemical equilibrium is not yet reached. Again, the hydrogen chemistry is less sensitive to recombination. As a consequence from the last observations, model PO is expected to deliver a higher wall heat flux due to the exothermic reactions dominating in the wall proximity. Scatter plots for cross-sections closer the outlet lead to similar conclusions and are not reported hereafter.
In order to directly compare models B and PO, the accessed composition space in terms of $(f, h)$ is shown in Fig. 9 for

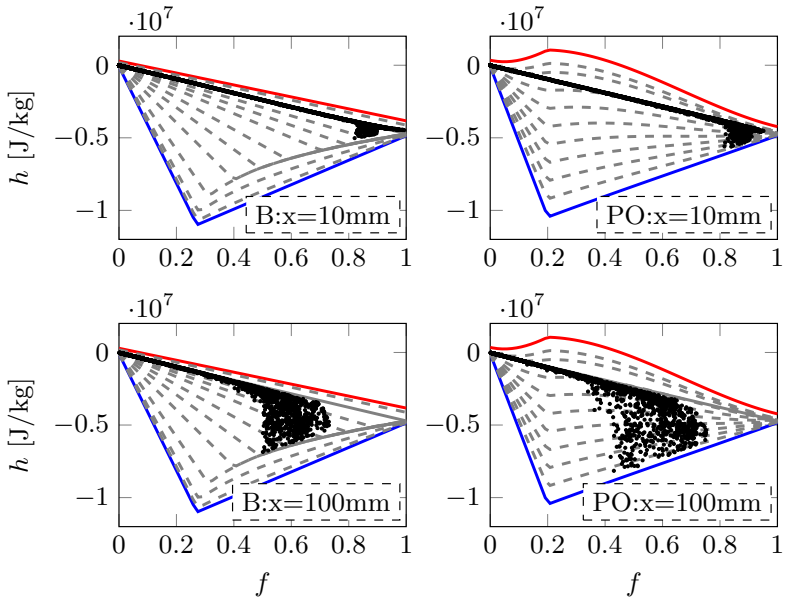


Figure 9: Scatter plots for absolute enthalpy $h$ over $f$ at cross sections x=10 and 100 mm

the same cross sections. Closer to the faceplate, the combustion regime is well represented by the adiabatic flamelet model. The clustered points at $f = 0.8$ for x = 10 mm are located in the recirculation zone, with more scattering present in PO. Moving downstream to x = 100 mm, the flame structure departures from the adiabatic state at the wall proximity. While the frozen chemistry states located in the lower region of table B are not accessed (states close to the blue line), the enthalpy space of table PO is accessed also in proximity of the lower boundary $h_{min}$. As a consequence, thermo-chemical states corresponding to a colder mixture are looked-up in table PO, located in the region where recombination reactions have almost completed.

**Comparison with Experimental Data**

The mean axial pressure and wall heat flux profiles for all simulations (B, PO, PM) are compared to the experimental results in Fig. 10. The non-cylindrical cross-section required circumferential averaging of the investigated fields over the four walls. The axial pressure profiles shown on the right are first discussed. A possible cause of mismatch in pressure profiles between different simulations is either the combustion model or the turbulence model. In this work the combustion model is based on the same tabulation method, non-adiabatic flamelets, which was found to have a minor influence on the core flow quantities. The IDDES turbulence model is also unvaried between the cases. Therefore it was expected that all CFD profiles would match. Moreover, they qualitatively follow the experimental distribution. The pressure peak in proximity of the injector is caused by the impact of the fuel jet at wall with a drop in velocity due to the recirculation zone. Afterwards the pressure decreases smoothly towards the assigned value at output.
More noteworthy is the wall heat flux prediction compared to the latest reconstruction from the inverse heat conduction problem[33] . The profile of case B is in very good agreement with the experiment, being entirely contained within the error bars or relatively close in the first part of the domain. Case PM is perfectly matching B, as anticipated in the previous section. The prediction in PO is overestimating the experiment because of the exothermic reactions at walls as discussed before. It should be noted however that the IDDES simulation improved the prediction of the heat flux for the PO method compared to the previous RANS computation[28] , lowering the peak from 10 MW/m$^2$ to about 6 MW/m$^2$ in the current work. This suggests that LES is more suitable than RANS for such configurations. To compensate the computational power required by the boundary layer resolved model, suitable temperature wall functions delivering a comparable accuracy in heat flux prediction will be further investigated in future work.

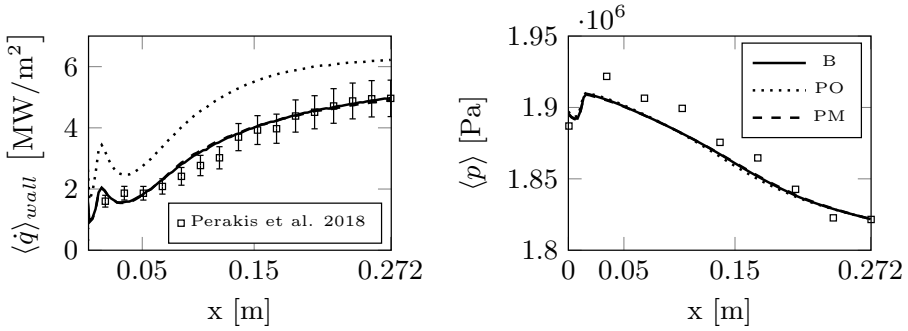


Figure 10: Axial pressure and wall heat flux compared to the experimental results

## Conclusions

A $GCH_4$-$GO_2$ single-injector combustion chamber was used to test the effects of using two different non-adiabatic flamelet models. The first model (named B) introduces a chemically-inert isothermal wall to induce side-wall flame quenching on the adiabatic flamelets. The second model (PO) solves the flamelet equations for species in mixture fraction space via an operation splitting technique, with the enthalpy profiles assigned in advance. A third model (PM) proves that model PO delivers the same results as model B, if the enthalpy profiles are taken from B. Regarding the computational time, model PO is more efficient, although CPU parallelization was applied in both cases. However, PO requires target enthalpy profiles as input, which should be chosen to cover the whole composition space of the CFD simulation. The best trade-off based on this work is delivered by model PM, which exploits the optimized routines of model PO but receives as input the enthalpy profiles of B.
A hybrid RANS/LES turbulence model (IDDES) was selected in OpenFOAM to simulate the $GCH_4/GO_2$ single-injector combustion chamber with tables B, PO and PM. While the core flow fields do not sensibly change between the three models, the major discrepancy is seen at walls where the heat losses preveal. The choice of the enthalpy space in PO has a larger effect on the recombination prediction than the scalar dissipation rate model has. Species recombination at walls is predicted by both models, but is enhanced in PO where the state approaches the chemical equilibrium. Model PM produces results coincident with B. The axial pressure distribution is qualitatively well predicted by all simulations, while the wall heat flux prediction of B (and therefore PM) is in excellent agreement with the experimental data. The IDDES turbulence model together with the non-adiabatic flamelet model B (or the modified PM) are capable of correctly predicting the experimental wall heat-flux of this test case.
Future work is targeted to optimize the lack of performance of model B while generating the tables. A suitable wall function capable of delivering a similar accuracy to the current numerical set-up is also topic of research.

## Acknowledgments

The first author gratefully acknowledges the Gauss Centre for Supercomputing e.V. (www.gauss-centre.eu) for funding this project by providing computing time on the GCS Supercomputer SuperMUC at Leibnitz Supercomputing Centre (LRZ, http://www.lrz.de).

## References

[1] J.P. Sutton and O. Biblarz. *Rocket Propulsion Elements*. John Wiley and Sons, 2010.

[2] T. Echekki and E. Mastorakos. *Turbulent Combustion Modeling*. Springer, 2011.

[3] N. Peters. Laminar diffusion flamelet models in non-premixed turbulent combustion. *Progress in Energy and Combustion Science*, 10:319–339, 1984.

[4] C.D. Pierce and P. Monin. Progress-variable approach for large-eddy simulation of non-premixed turbulent combustion. *Journal of Fluid Mechanics*, 504:73–97, 2004.

[5] J.A.van Oijen and L.P.H. de Goey. Modeling of premixed laminar flames using flamelet-generated manifolds. *Combustion Science and Technology*, 88:239–264, 1992.

[6] D.J. Lee, S. Thakur, J. Wright, M. Ihme, and W. Shyy. Charachterization of flow field structure and species composition in a shear coaxial rocket gh2/go2 injector: Modeling of wall heat losses. AIAA Paper 2017-6125, American Institute of Aeronautics and Astronautics, July 2011.

[7] H. Wu and M. Ihme. Modeling of wall heat transfer and flame/wall interaction a flamelet model with heat-loss effects. Conference paper, 9th U.S. National Combustion Meeting, May 2015.

[8] P.C. Ma, H. Wu, M. Ihme, and J.P. Hickey. A flamelet model with heat-loss effects for predicting wall-heat transfer in rocket engines. AIAA Paper 2017-4856, American Institute of Aeronautics and Astronautics, July 2017.

[9] P.C. Ma, H. Wu, and M. Ihme. Nonadiabatic flamelet formulation for predicting wall heat transfer in rocket engines. *AIAA Journal*, 56(6):2336–2349, June 2018.

[10] P. Breda, J. Zips, and M. Pfitzner. A non-adiabatic flamelet approach for non-premixed o2/ch4 combustion. Conference paper, Proceeding of the 3rd World Congress on Momentum, Heat and Mass Transfer, 2018.

[11] J. Zips, C. Traxinger, P. Breda, and M. Pfitzner. Assessment of presumed/transported probability density fuction methods for rocket combustion simulations. *Journal of Propulsion and Power*, pages 1–19, 2019.

[12] S-K. Kim, M. Joh, H.S. Choi, and T. S. Park. Multidisciplinary simulation of a regeneratively cooled thrust chamber of liquid rocket engine: Turbulent combustion and nozzle flow. *International Journal of Heat and Mass Transfer*, 70:1066–1077, 2014.

[13] D. Rahn, O.J. Haidn, H. Riedmann, and R. Behr. Non-adiabatic flamelet modeling for the numerical simulation of methane combustion in rocket thrust chambers. AIAA Paper 2018-4869, American Institute of Aeronautics and Astronautics, July 2018.

[14] N. Perakis, C. Roth, and O.J. Haidn. Development of a non-adiabatic flamelet model for reacting flows with heat loss. Conference Paper SP2018-00171, Space Propulsion, May 2018.

[15] H.G. Weller, G. Tabor, H. Jasak, and C. Fureby. A tensorial approach to computational continuum mechanics using object-oriented techniques. *Computers in Physics*, 12(6), Nov/Dec 1998.

[16] D.G. Goodwin, R.L. Speth, H.K. Moffat, and B.W. Weber. Cantera: An object-oriented software toolkit for chemical kinetics, thermodynamics, and transport processes. https://www.cantera.org, 2018.

[17] O.J. Haidn, M.P. Celano, S. Silvestri, C. Kirchberger, and G. Schlieben. Test case 1: Single element combustion chamber - gch4/gox transregio sfb-tr40 test case 1. Technical report, 2015.

[18] M.L. Shur, P.R. Spalart, M.K. Strelets, and A.K. Travin. A hybrid rans-les approach with delayed-des and wall-modelled les capabilities. *International Journal of Heat and Fluid Flow*, 29(6):1638–1649, 2008.

[19] P. Spalart and S. Allmaras. A one-equation turbulence model for aerodynamic flows. *La Recherche Aerospatiale*, 1(1):5–21, 1994.

[20] R. Sankaran, E. Hawkes, J. Chen, T. Lu, and C.K. Law. Structure of a spatially developing turbulent lean methane/air bunsen flame. *Proceedings of the Combustion Institute*, 31(1):1291–1298, January 2007.

[21] M. Frenklach et al. Gri-mech—an optimized detailed chemical reaction mechanism for methane combustion. Report GRI-95/0058, November 1995.

[22] D. Maestro, B. Cuenot, and L. Selle. Large eddy simulation of flow and combustion in a single-element gch4/gox rocket combustor. Conference paper, 7th European Conference for Aeronautics and Aerospace Sciences, 2017.

[23] K. Kemenov, H. Wang, and S. Pope. Modelling effects of subgrid-scale mixture fraction variance in les of a piloted diffusion flame. *Combustion Theory and Modelling*, 16(4):611–638, 2014.

[24] P. Domingo, L. Vervisch, and D. Veynante. Large-eddy simulation of a lifted methane jet flame in vitiated coflow. *Combustion and Flame*, 152:415–432, 2008.

[25] M.P. Celano at al. Injector characterization for a gaseous oxygen-methane single element combustion chamber. *Progress in Propulsion and Power*, 8:145–164, 2016.

[26] P.E. Lapenna et al. Simulation of a single-element gch4/gox rocket combustor using a non-adiabatic flamelet method. AIAA Paper 2018-4872, American Institute of Aeronautics and Astronautics, July 2018.

[27] H. Müller et al. Numerical investigation of flow and combustion in a single-element gch4/gox rocket combustor: A comparative les study. AIAA Paper 2016-4997, American Institute of Aeronautics and Astronautics, July 2016.

[28] N. Perakis, C. Roth, and O.J. Haidn. Simulation of a single-element rocket combustor using a non-adiabatic flamelet model. Conference Paper SP2018-00174, Space Propulsion, May 2018.

[29] C. Roth at al. Numerical investigation of flow and combustion in a single-element gch4/gox rocket combustor. Conference Paper 2016-4995, American Institute of Aeronautics and Astronautics, July 2016.

[30] J. Zips, H. Müller, and M. Pfitzner. Non-adiabatic tabulation methods to predict wall-heat loads in rocket combustion. Conference Paper 2017-1469, IAA SciTech Forum, Jan 2017.

[31] F. Winter, N. Perakis, and O.J. Haidn. Emission imaging and cfd simulation of a coaxial single-element gox/gch4 rocket combustor. AIAA Paper 2018-4764, American Institute of Aeronautics and Astronautics, 2018.

[32] M.C Immer. *Time-resolved measurement and simulation of local scale turbulent urban flow*. PhD thesis, ETH Zürich, 2016.

[33] N. Perakis and O.J. Haidn. Inverse heat transfer method applied to capacitiverly cooled rocket thrust chambers. *International Journal of Heat and Mass Transfer*, 131:150–166, 2019.